Screening binary alloys for electrochemical CO_2 reduction towards multi-carbon products

Jiang Li[a,b], Joakim Halldin Stenlid[a,b], Michael T. Tang[a,b], Hongjie Peng[a,b], Frank Abild-Pedersen[b,*]

[a]*SUNCAT Center for Interface Science and Catalysis, Department of Chemical Engineering, Stanford University, Stanford, CA 94305, USA*

[b]*SUNCAT Center for Interface Science and Catalysis, SLAC National Accelerator Laboratory, 2575 Sand Hill Road, Menlo Park, California 94025, United States*

**Corresponding author: abild@slac.stanford.edu*

Supporting Information

Supplementary Note 1: Gibbs free energy correction

To directly obtain the reaction energies ΔG_{rxn} from energetic scaling relationship and use them for the selectivity maps, we used adsorption free energies, G, instead of electronic energies to construct those scaling relationships. G is affected by the selected gas phase free energies as the references. Here we made the same assumption as Peterson et al.[1] did in 2010 that gaseous products in the pathway were calculated at partial pressures corresponding to the Faradaic yields reported by Hori et al.[2]. In our previous paper,[3-4] we provided details of free energy calculations of gas phases, including the assumed fugacity for gas phases, along with calculated electronic energies (E_{raw}), DFT correction ($E_{BEEF\text{-}vdW}$), corrected electronic energies ($E_{ele} = E_{raw} + E_{BEEF\text{-}vdW}$), zero-point energies (ZPE), enthalpic temperature correction ($\int C_p dT$), entropy contribution ($-TS$), chemical potential ($\mu = E_{ele} + ZPE + \int C_p dT - TS$), and the total correction ($\mu - E_{ele} = ZPE + \int C_p dT - TS$). The free energy corrections of gas phase references CO(g), H2O(g), and H2(g) are provided in **Table S1**.

Table S1. Free energy corrections of gas phase references.[3-4]

Species	Fugacity (Pa)	E_{raw} (eV)	$E_{BEEF\text{-}vdW}$ (eV)	E_{ele} (eV)	ZPE (eV)	$\int C_p dT$ (eV)	$-TS$ (eV)	μ (eV)	$\mu - E_{ele}$ (eV)
CO(g)	5562	0.00		0.00	0.13	0.09	−0.69	−0.46	−0.46
H_2O(g)	3534	0.00		0.00	0.57	0.10	−0.67	0.00	0.00
H_2(g)	101325	−0.09	0.09	0.00	0.27	0.09	−0.40	−0.04	−0.04

Reaction energetics are given relative to gas-phase CO, H_2O, and H_2. Besides, an overbinding correction to CO adsorption energy was applied, except the cases where CO is adsorbed on coinage metals (Cu, Ag, Au) top sites. This is done since generalized gradient approximations (GGA) functionals generally position the unfilled 2π* orbital at a too low energy relative to the metal d-

states. The overbinding correction can be estimated from the harmonic vibrational frequencies for the CO* internal stretch mode (ν_{co}), i.e., $E_{CO\text{-}overbinding} = 1.8 - 0.0008\nu_{co}$.[5]

Table S2 Adsorption free energies of CO* and C* on pure metal (100) surfaces.

Metal (100)	ν_{co} (cm^{-1})	$E_{CO\text{-}overbinding}$ (eV)	$ZPE_{CO*@top}$ (eV)	$ZPE_{C*@4\text{-}fold}$ (eV)	$G_{CO*@top}$ (eV)	$G_{C*@4\text{-}fold}$ (eV)
Fe	1939.9	0.248	0.221	0.073	-0.425	-0.164
Co	1986.4	0.211	0.212	0.093	-0.778	-0.755
Ni	2039.3	0.169	0.199	0.101	-0.816	-1.057
Mo	1943	0.246	0.185	0.09	-0.781	-2.135
Ru	1993.4	0.205	0.222	0.089	-1.097	-1.194
Rh	2001.7	0.199	0.229	0.082	-1.024	-1.025
Pd	2045.6	0.164	0.178	0.089	-0.534	-0.718
W	1944.9	0.244	0.185	0.099	-1.008	-2.912
Re	1963.8	0.229	0.242	0.097	-1.307	-2.615
Os	2002.1	0.198	0.234	0.089	-1.400	-1.423
Ir	2031.3	0.175	0.254	0.083	-1.353	-1.006
Pt	2075	0.140	0.204	0.084	-0.968	-0.476
Cu	2055.5	0.000	0.178	0.093	-0.100	0.956
Zn	2025.4	0.180	0.161	0.079	0.608	1.150
Ag	2074.5	0.000	0.171	0.069	0.383	2.885
Au	2073.1	0.000	0.178	0.068	0.325	2.512
Al	1972.9	0.222	0.170	0.08	0.534	0.191
Ga	2143.6	0.085	0.164	0.053	0.537	1.848
In	2143.6	0.085	0.180	0.051	0.543	2.419
Si	1972.4	0.222	0.199	0.081	0.677	1.103
Ge	2150.8	0.079	0.174	0.065	0.516	1.729
Sn	2150.2	0.080	0.188	0.062	0.530	2.138
Pb	2149	0.081	0.158	0.057	0.542	2.576
As	1962.6	0.230	0.215	0.078	0.729	0.154
Sb	2138.3	0.089	0.183	0.069	-1.893	0.698
Bi	2147.1	0.082	0.157	0.059	0.540	1.784

In this work, we have calculated the ZPE of CO* and C* on different metal surfaces and found that ZPE varies very little for the different metals. The mean value of the $ZPE_{CO*@top}$ is 0.194 eV with a standard deviation of 0.027 eV; the mean value of the $ZPE_{C*@4\text{-}fold}$ is 0.078 eV with a standard deviation of 0.014 eV. In this work, we therefore apply free energy corrections for CO* of 0.53 eV and for C* of 0.57 eV as calculated on Cu(100), as a correction to all the CO* and C* adsorption energies calculated on different metal and metal alloy (**Table S2** and **S3**) surfaces (free adsorption energy is obtained by adding the free energy correction and overbinding correction (for CO) to the calculated potential adsorption energy). These specific free energy corrections of 0.53

eV for CO* and 0.57 eV for C* on Cu(100) have also been extrapolated and applied in our previous work.[4] We note, that the CO* adsorption energy on pure Sb is abnormal compared with other p-block elements, which is a consequence of severe surface disorder of Sb due to the CO* adsorption event. This Sb data point was not included in **Figure 2** in the main text.

Table S3 Adsorption free adsorption energy of CO* and C* on the (100) surface of the $L1_2$ alloy. $E_{CO\text{-overbinding}}$ for CO adsorption on the atop site of the alloy surface is approximated by the overbinding correction of CO on pure metal listed in **Table S2**.

$L1_2$ alloy (100)	$E_{CO\text{-overbinding}}$ (eV)	$G_{CO*@top}$ (eV)	$G_{C*@4\text{-fold}}$ (eV)
Cu_3Fe	0.248	-0.381	0.041
Cu_3Co	0.211	-1.038	-0.848
Cu_3Ni	0.169	-0.924	-0.605
Cu_3Mo	0.246	-1.085	-2.020
Cu_3Ru	0.205	-1.398	-1.552
Cu_3Rh	0.199	-1.160	-1.143
Cu_3Pd	0.164	-0.229	0.836
Cu_3W	0.244	-1.310	-2.349
Cu_3Re	0.229	-1.774	-2.655
Cu_3Os	0.198	-1.953	-2.451
Cu_3Ir	0.175	-1.592	-1.658
Cu_3Pt	0.140	-0.678	0.180
Cu_3Zn	0.000	-0.116	1.568
Cu_3Ag	0.000	-0.059	1.693
Cu_3Au	0.000	-0.018	1.741
Cu_3Al	0.000	0.007	0.313
Cu_3Ga	0.000	0.043	1.168
Cu_3In	0.000	0.114	1.625
Cu_3Si	0.000	-0.060	0.248
Cu_3Ge	0.000	-0.002	0.948
Cu_3Sn	0.000	0.164	1.477
Cu_3Pb	0.000	0.094	1.771
Cu_3As	0.000	-0.082	2.202
Cu_3Sb	0.000	0.100	2.265
Cu_3Bi	0.000	0.079	2.355
Zn_3Fe	0.248	-0.813	0.013
Ag_3Fe	0.248	-1.296	-1.357
Au_3Fe	0.248	-1.092	-0.929
Al_3Fe	0.248	-0.649	-0.358
Ga_3Fe	0.248	-0.336	0.990
In_3Fe	0.248	-0.875	-0.229
Si_3Fe	0.248	0.116	0.656
Ge_3Fe	0.248	-0.362	-1.435
Sn_3Fe	0.248	-0.076	0.022

Pb_3Fe	0.248	-1.272	-1.149
Zn_3Co	0.211	-0.893	-0.147
Ag_3Co	0.211	-0.995	-0.131
Au_3Co	0.211	-1.235	-1.053
Al_3Co	0.211	-0.756	-0.329
Ga_3Co	0.211	-0.637	0.371
In_3Co	0.211	-0.645	-0.335
Ge_3Co	0.211	-0.675	-1.906
Sb_3Co	0.211	-2.203	1.320
Zn_3Ni	0.169	-0.625	0.456
Ag_3Ni	0.169	-1.065	-0.106
Au_3Ni	0.169	-0.958	0.047
Al_3Ni	0.169	-0.245	0.072
Ga_3Ni	0.169	-0.420	0.720
In_3Ni	0.169	-0.824	0.106
Si_3Ni	0.169	-0.521	-2.414
Pb_3Ni	0.169	-1.330	-0.292
Zn_3Pd	0.164	0.114	1.689
Ag_3Pd	0.164	-0.334	1.492
Au_3Pd	0.164	-0.350	1.146
Al_3Pd	0.164	0.401	0.663
Ga_3Pd	0.164	0.162	1.376
In_3Pd	0.164	-0.013	1.917
Si_3Pd	0.164	-0.515	-1.341
Ge_3Pd	0.164	-0.125	0.834
Sn_3Pd	0.164	-0.220	0.765
Pb_3Pd	0.164	-0.224	1.409
As_3Pd	0.164	-1.422	-1.815
Bi_3Pd	0.164	-1.363	0.481

Table S4 Adsorption free energy of CO* and C* on $L1_0$ alloy (110) surfaces. There are two kinds of 4-fold sites on the (110) surface of the $L1_0$ alloy for C* adsorption, and we use the most stable of the two adsorption sites in our selectivity map in **Figure 3** in the main text.

$L1_2$ alloy (100)	$E_{CO\text{-}overbinding}$ (eV)	$G_{CO*@top}$ (eV)	$G_{C*@4\text{-}fold\text{-}1}$ (eV)	$G_{C*@4\text{-}fold\text{-}2}$ (eV)
CuFe	0.248	-0.391	0.321	0.306
CuCo	0.211	-0.896	-0.161	0.500
CuNi	0.169	-0.924	-0.159	-0.019
CuMo	0.246	-0.927	-1.032	-0.953
CuRu	0.205	-1.228	-0.694	-0.496
CuRh	0.199	-1.133	-0.609	-0.664
CuPd	0.164	-0.401	1.027	0.573
CuW	0.244	-1.036	-1.390	-1.139
CuRe	0.229	-1.018	-1.965	-1.617
CuOs	0.198	-1.222	-1.033	0.007
CuIr	0.175	-1.510	-1.028	-0.392
CuPt	0.140	-0.916	0.213	0.419
CuZn	0.000	0.039	1.537	1.408
CuAg	0.000	-0.091	2.903	1.823
CuAu	0.000	-0.063	2.628	2.033
CuAl	0.000	0.359	1.362	0.933
CuGa	0.000	0.221	1.545	1.508
CuIn	0.000	0.171	2.990	1.564
CuGe	0.000	-0.036	1.054	1.439
CuSn	0.000	0.114	3.132	1.533
CuAs	0.000	-0.010	0.286	0.663
FeZn	0.248	-0.378	0.659	0.649
FeAl	0.248	-0.836	0.731	-0.012
FeGa	0.248	-0.341	0.708	0.797
FeSi	0.248	-0.522	1.206	1.467
FeGe	0.248	-0.562	2.385	1.426
FePb	0.248	-0.077	1.164	1.234
FeAs	0.248	0.298	1.203	0.998
CoZn	0.211	-1.115	1.090	-0.118
CoAg	0.211	-0.809	1.961	-0.431
CoAl	0.211	-1.257	1.186	0.014
CoGa	0.211	-0.991	1.927	0.614
CoSi	0.211	-0.137	1.309	1.833
CoGe	0.211	-0.320	2.568	1.383
CoSn	0.211	-0.530	3.588	0.884
CoPb	0.211	-0.490	3.410	-0.444
CoAs	0.211	-0.359	2.626	1.133
CoSb	0.211	-0.416	3.636	1.188
NiZn	0.169	-0.749	1.603	0.809

NiAg	0.169	-1.002	1.665	0.088
NiAl	0.169	-0.325	1.553	0.653
NiGa	0.169	-0.209	2.115	1.269
NiIn	0.169	-0.428	2.998	0.882
NiSi	0.169	0.199	1.358	1.759
NiGe	0.169	-0.061	2.624	1.577
NiAs	0.169	-0.231	0.915	1.632
NiBi	0.169	-0.593	3.778	0.636
PdZn	0.164	-0.035	1.992	2.523
PdAg	0.164	-0.475	1.191	1.121
PdAu	0.164	-0.451	0.847	1.065
PdAl	0.164	0.336	1.521	2.371
PdGa	0.164	0.315	1.988	2.454
PdIn	0.164	0.232	3.286	2.304
PdSi	0.164	0.466	0.984	1.462
PdGe	0.164	0.251	1.520	2.049
PdSn	0.164	0.274	3.494	2.368
PdPb	0.164	0.072	4.018	1.983
PdAs	0.164	0.072	1.364	2.597
PdSb	0.164	0.222	3.087	2.507
PdBi	0.164	0.028	3.559	2.466

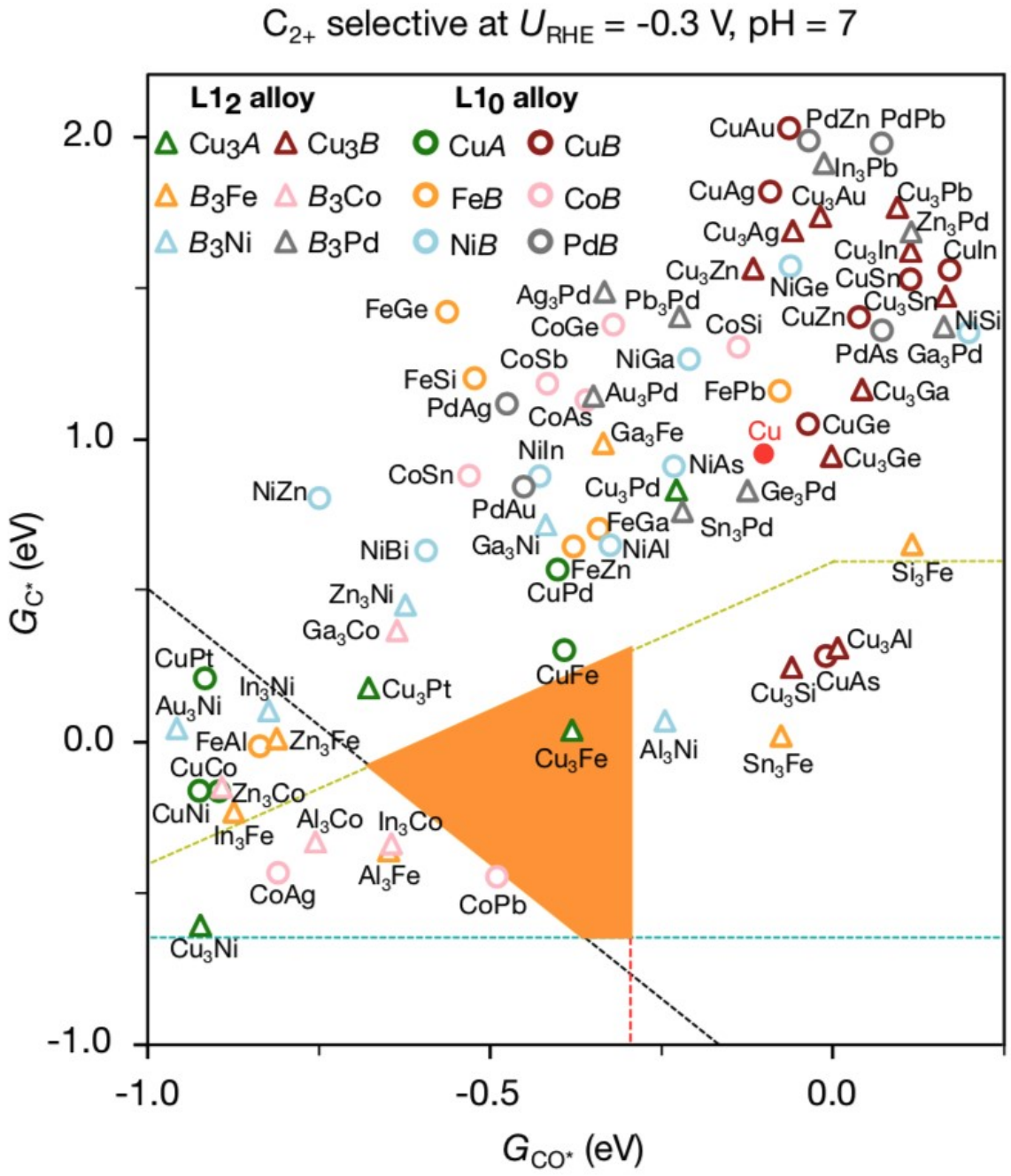

Figure S1 Selectivity map of $L1_2(100)$ and $L1_0(110)$ surfaces at -0.3 V (vs. RHE) at pH 7. The triangle markers denote the $L1_2$ binary alloys of Cu_3A (green), Cu_3B (dark red), B_3Fe (orange), B_3Co (pink), B_3Ni (light blue), and B_3Pd (gray). The circle ones are the $L1_0$ alloys of Cu*A* (green), Cu*B*(dark red), *B*Fe (orange), *B*Co (pink), *B*Ni (light blue), and BPd (gray).

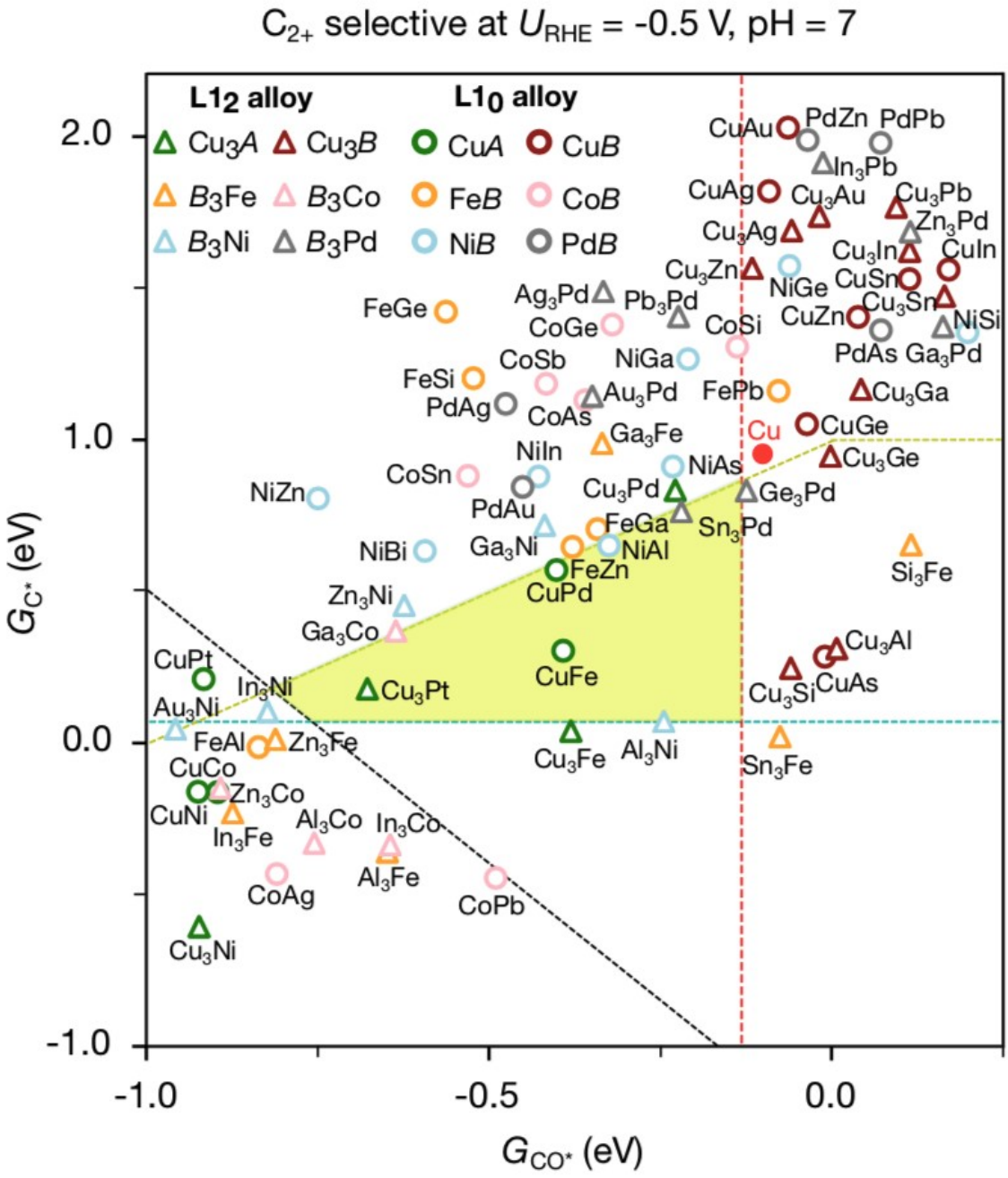

Figure S2 Selectivity map of $L1_2(100)$ and $L1_0(110)$ surfaces at -0.5 V (vs. RHE) at pH 7. The triangle markers denote the $L1_2$ binary alloys of Cu_3A (green), Cu_3B (dark red), B_3Fe (orange), B_3Co (pink), B_3Ni (light blue), and B_3Pd (gray). The circle ones are the $L1_0$ alloys of Cu*A* (green), Cu*B*(dark red), *B*Fe (orange), *B*Co (pink), *B*Ni (light blue), and BPd (gray).

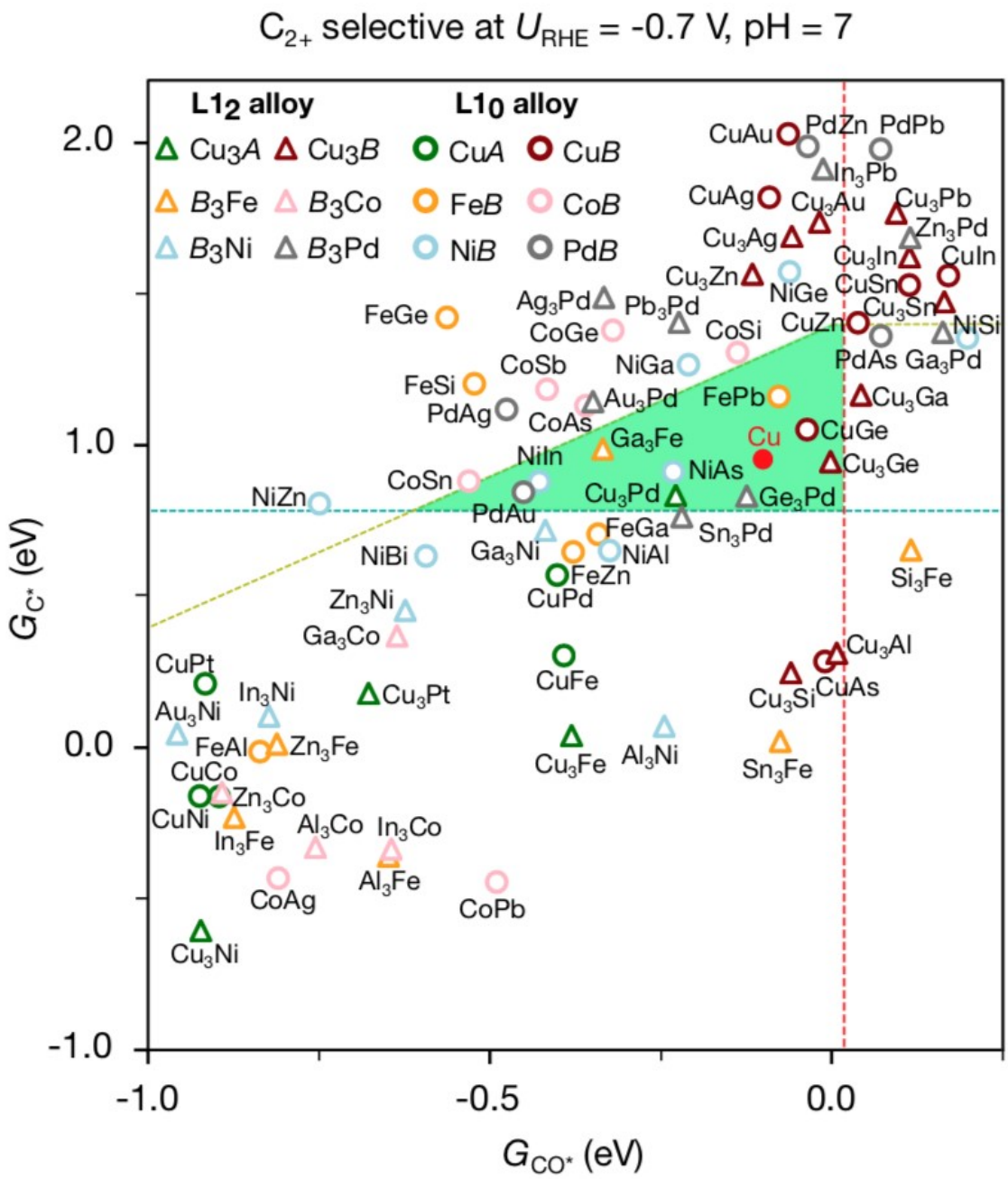

Figure S3 Selectivity map of $L1_2(100)$ and $L1_0(110)$ surfaces at -0.7 V (vs. RHE) at pH 7. The triangle markers denote the $L1_2$ binary alloys of Cu_3A (green), Cu_3B (dark red), B_3Fe (orange), B_3Co (pink), B_3Ni (light blue), and B_3Pd (gray). The circle ones are the $L1_0$ alloys of Cu*A* (green), Cu*B*(dark red), *B*Fe (orange), *B*Co (pink), *B*Ni (light blue), and BPd (gray).

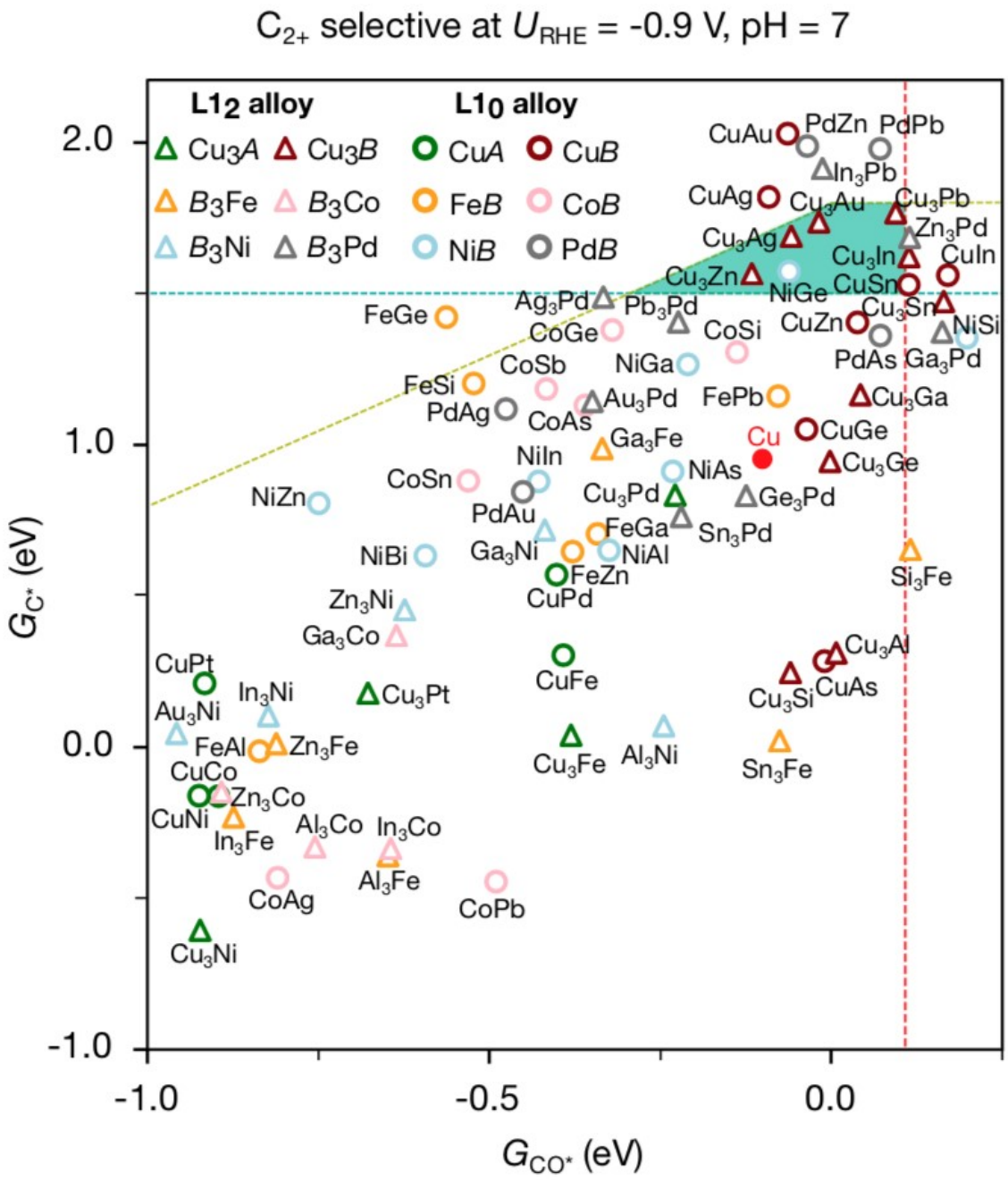

Figure S4 Selectivity map of $L1_2(100)$ and $L1_0(110)$ surfaces at -0.9 V (vs. RHE) at pH 7. The triangle markers denote the $L1_2$ binary alloys of Cu_3A (green), Cu_3B (dark red), B_3Fe (orange), B_3Co (pink), B_3Ni (light blue), and B_3Pd (gray). The circle ones are the $L1_0$ alloys of Cu*A* (green), Cu*B*(dark red), *B*Fe (orange), *B*Co (pink), *B*Ni (light blue), and BPd (gray).

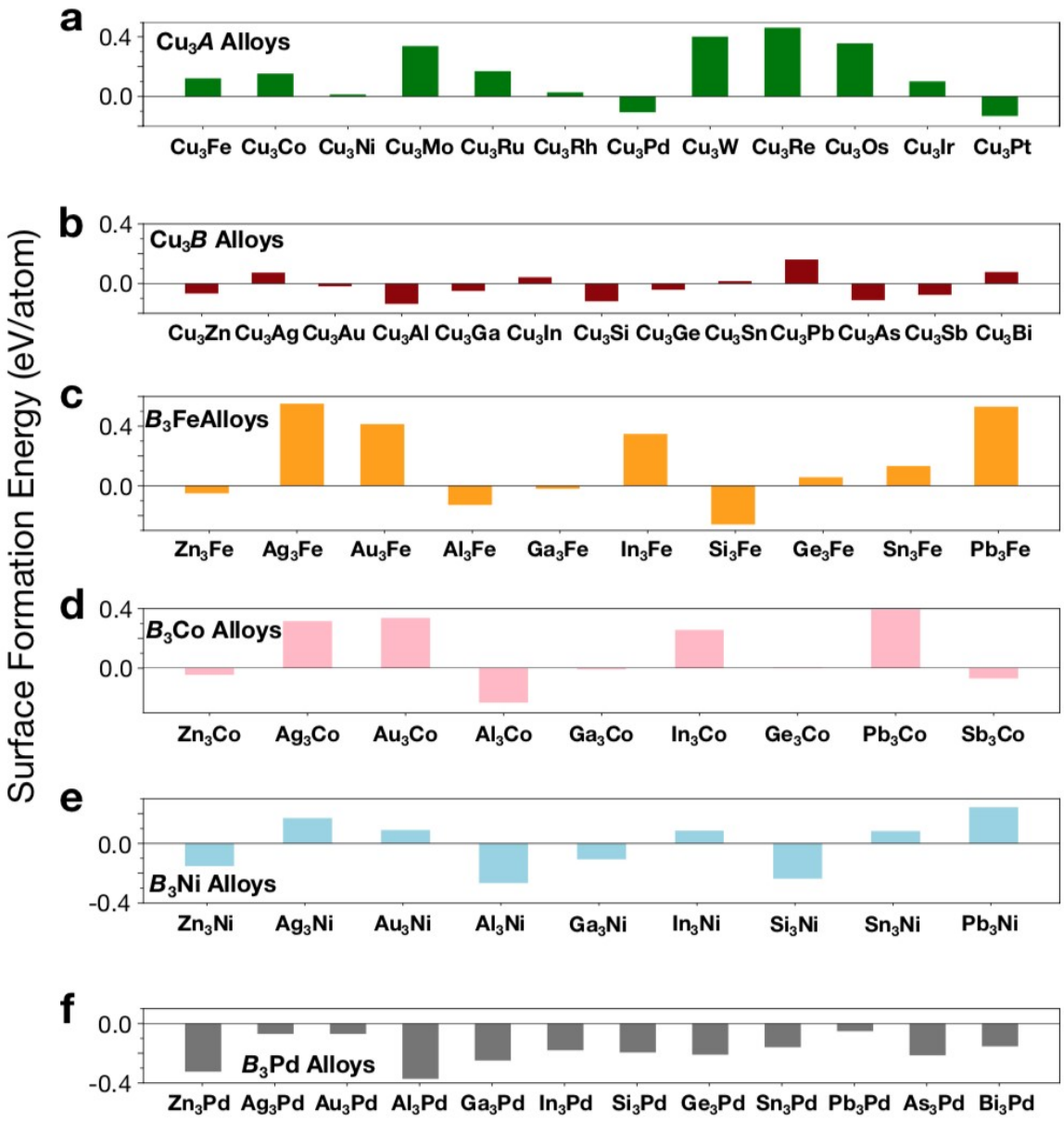

Figure S5 Segregation energies of clean (100) surfaces of $L1_2$ binary alloys. (a) Cu_3A alloys, (b) Cu_3B alloys, (c) B_3Fe alloys, (d) B_3Co Alloys, (e) B_3Ni alloys, and (f) B_3Pd alloys. *A* represents strong CO binding metals (Fe, Co, Ni, Pd, Pt, Mo, Ru, Rh, W, Re, Os, Ir) and *B* represents weak CO binding metals (Zn, Ag, Au, Al, Ga, In, Si, Ge, Sn, Pb, As, Sb, Bi). Some of the binary alloys, mainly the Fe, Co, and Ni-based alloys, are not shown in the figure because of the severe restructuring or decomposing during the DFT geometric optimization. Consequently, these missing alloys are considered unstable.

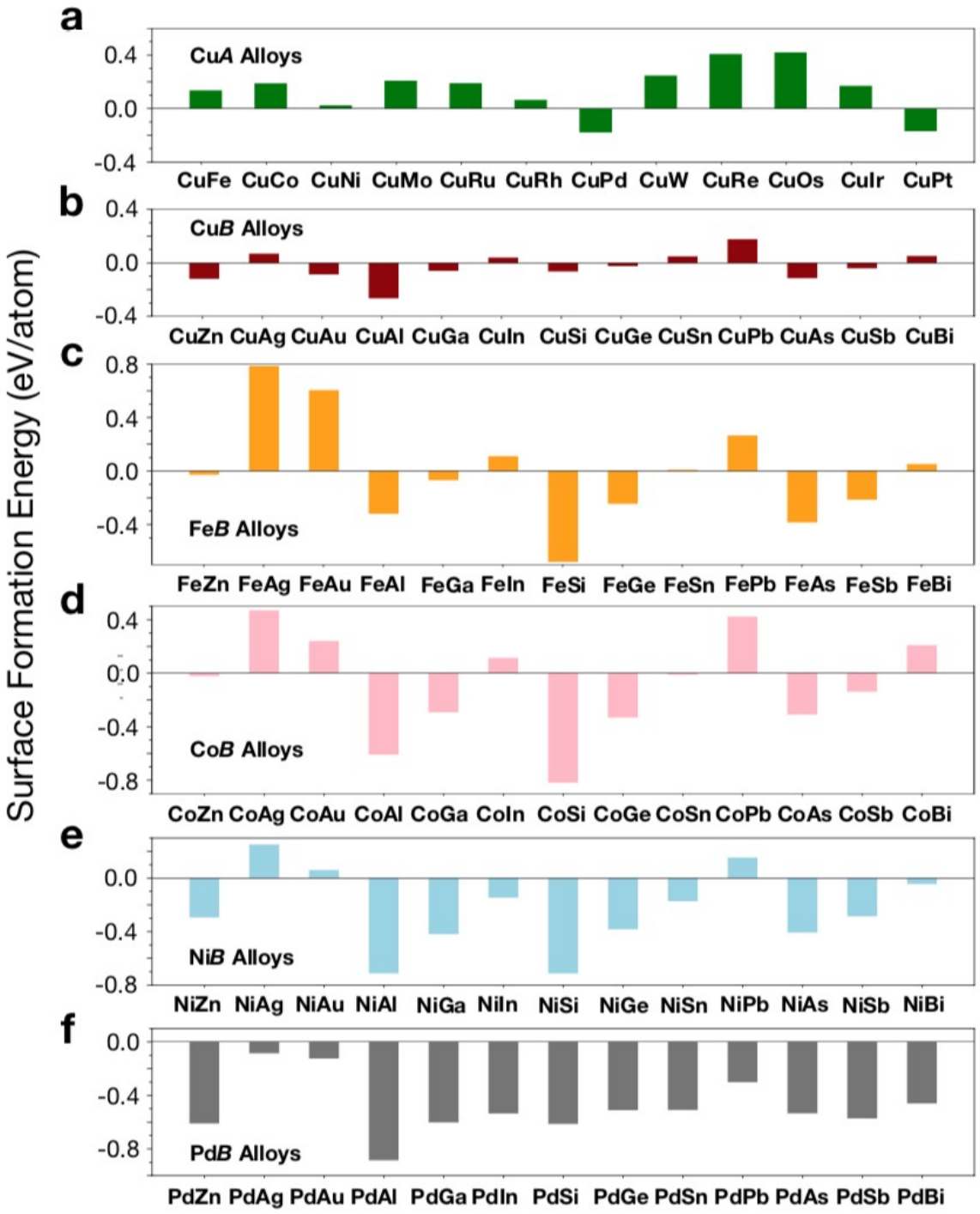

Figure S6 Segregation energies of clean (110) surfaces of $L1_0$ binary alloys. (a) Cu*A* alloys, (b) Cu*B* alloys, (c) Fe*B* alloys, (d) Co*B* Alloys, (e) Ni*B* alloys, and (f) Pd*B* alloys. *A* represents strong CO binding metals (Fe, Co, Ni, Pd, Pt, Mo, Ru, Rh, W, Re, Os, Ir) and *B* represents weak CO binding metals (Zn, Ag, Au, Al, Ga, In, Si, Ge, Sn, Pb, As, Sb, Bi). Some of the binary alloys, mainly the Fe, Co, and Ni-based alloys, are not shown in the figure because of the severe restructuring or decomposing during the DFT geometric optimization. Consequently, these missing alloys are considered unstable.

Reference

(1) Peterson, A. A.; Abild-Pedersen, F.; Studt, F.; Rossmeisl, J.; Nørskov, J. K. How copper catalyzes the electroreduction of carbon dioxide into hydrocarbon fuels. *Energy Environ. Sci.* **2010,** *3*, 1311-1315.

(2) Hori, Y.; Murata, A.; Takahashi, R. Formation of hydrocarbons in the electrochemical reduction of carbon dioxide at a copper electrode in aqueous solution. *J. Chem. Soc., Faraday Trans.1* **1989,** *85*, 2309-2326.

(3) Tang, M. T.; Peng, H.; Lamoureux, P. S.; Bajdich, M.; Abild-Pedersen, F. From electricity to fuels: Descriptors for C1 selectivity in electrochemical CO_2 reduction. *Appl. Catal. B* **2020,** *279*, 119384.

(4) Peng, H.; Tang, M. T.; Liu, X.; Lamoureux, P. S.; Bajdich, M.; Abild-Pedersen, F. The role of atomic carbon in directing electrochemical $CO_{(2)}$ reduction to multicarbon products. *Energy Environ. Sci.* **2021,** *14*, 473-482.

(5) Abild-Pedersen, F.; Andersson, M. P. CO adsorption energies on metals with correction for high coordination adsorption sites–A density functional study. *Surf. Sci.* **2007,** *601*, 1747-1753.